Science Advances

$\blacktriangleright$AAAS

Supplementary Materials for

Room temperature strain-induced Landau levels in graphene on a wafer-scale platform

P. Nigge, A. C. Qu, É. Lantagne-Hurtubise, E. Mårsell, S. Link, G. Tom, M. Zonno, M. Michiardi, M. Schneider, S. Zhdanovich, G. Levy, U. Starke, C. Gutiérrez, D. Bonn, S. A. Burke*, M. Franz*, A. Damascelli*

*Corresponding author. Email: saburke@phas.ubc.ca (S.A.B.); franz@physics.ubc.ca (M.F.); damascelli@physics.ubc.ca (A.D.)

This PDF file includes:

Supplementary materials

1. Extraction of Fermi velocity and quasiparticle lifetime from ARPES data

The Fermi velocity and binding energy dependence of the carriers can be directly extracted from the ARPES data. The momentum distribution curves (MDCs) at each binding energy are fitted using a Lorentzian with a constant background. Firstly, the dispersion of the band can then be fitted linearly to determine the Fermi velocity to $v_F = (9.50 \pm 0.08) \times 10^5 \text{ ms}^{-1}$ (see fig. S1A). Secondly, the width of the Lorentzians as a function of binding energy can be fitted quadratically with a constant offset. The linewidth is inversely proportional to the quasiparticle lifetime, thus showing how the latter *decreases* as one goes away from the Fermi level (see fig. S1B). This is a manifestation of a simple Fermi liquid model. Electrons at the Fermi level have a certain lifetime between scattering events dictated by the concentration of impurities and defects. As one goes to higher binding energies, the phase space for electron-electron scattering increases $\propto E_b^2$ and the lifetime decreases. We propose this as the reason why, experimentally,
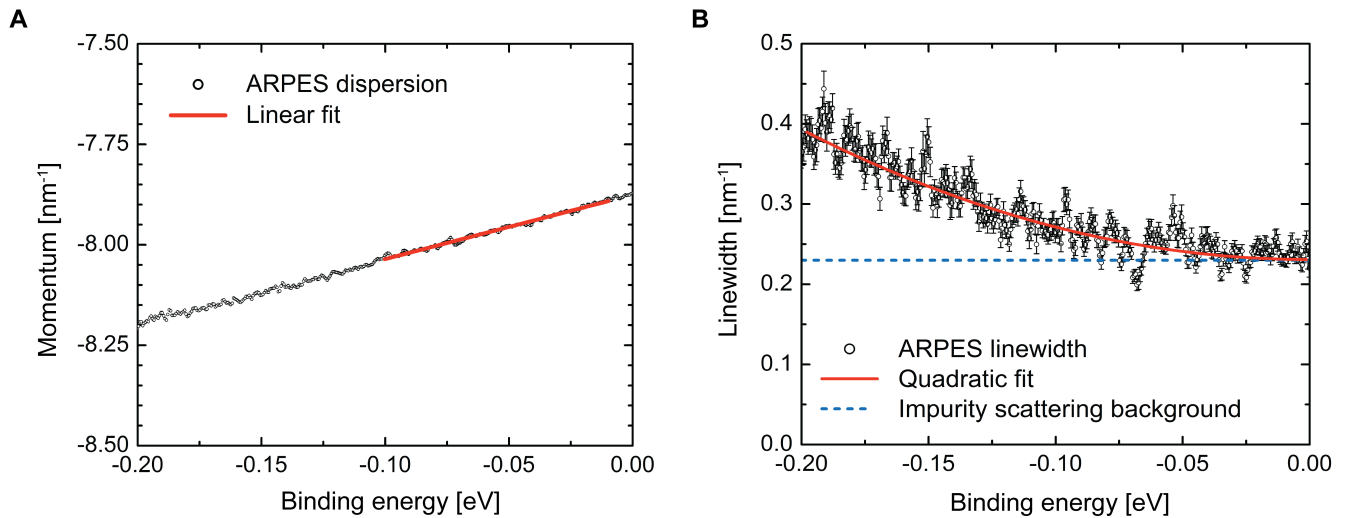
A

B

Fig. S1. Fermi velocity and quasiparticle lifetime from ARPES. (**A**) The linear dispersion of graphene (black circles) is fitted linearly (red line) to extract the Fermi velocity. (**B**) The extracted binding energy dependent linewidth (black circles) is fitted quadratically (red line) to illustrate the *decreasing* carrier lifetime at higher binding energies. The blue dashed line indicates a constant offset due to impurity scattering.

our LLs are only clearly resolved in the upper part of the cone closer to the Fermi level. When the scattering rate at some binding energy exceeds a critical value above which coherent circular orbits cannot be established, the LL quantization in the ARPES measurement disappears. We note that such asymmetric behaviour has been reported before in scanning probe measurements, and was attributed to a shorter vertical extension of wave functions at lower energies (*11*) and to a reduced quasiparticle lifetime away from the Fermi level as well (*27*).

2. Evolution of LLs with magnetic field strength

In fig. S2, we present the spectral function obtained for $M = 0$ and increasing pseudomagnetic fields $B = 0, 41, 82$ and 164 T to highlight how Landau levels evolve from a Dirac cone when $B = 0$ to completely flat bands when $l_B \ll \lambda$. This is analogous to keeping B fixed and increasing the size of the flake, but the latter method is strongly constrained by numerical resources. Here $l_B = 4.0, 2.8$ and 2.0 nm at $B = 41, 82$ and 164 T respectively, whereas $\lambda \sim 30$ nm.
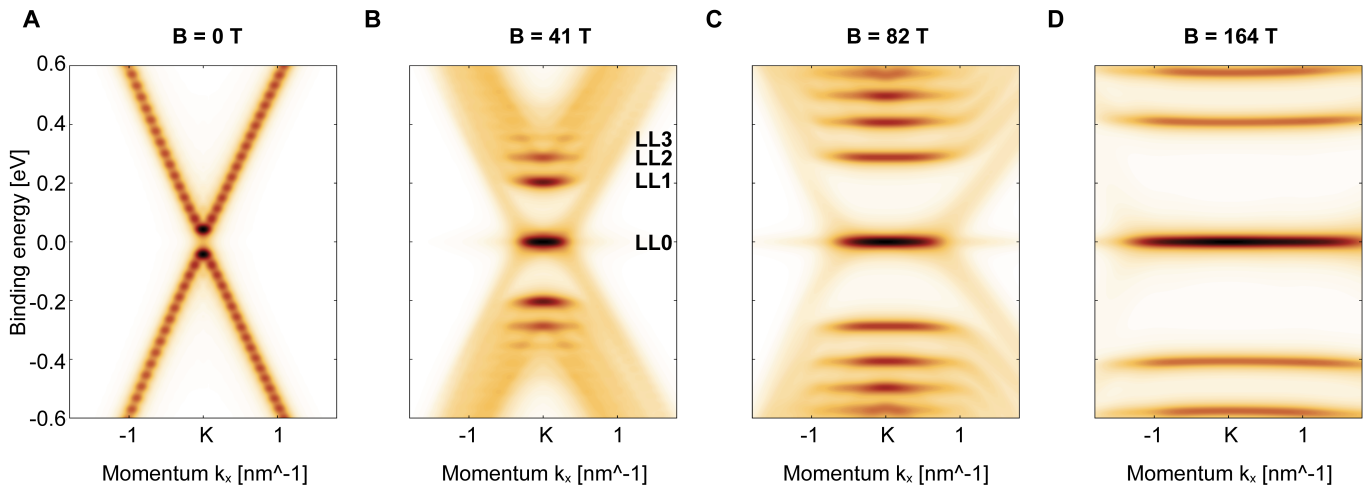

Fig. S2. Evolution of LLs for increasing uniform pseudomagnetic fields. Calculated spectral function in our triangular flake for fields $B = 0, 41, 82$ and 164 T (from left to right).

3. Effect of *uniform* mass term on LL spectrum

Here we briefly discuss the effect of a Semenoff mass (*35*) M on pseudo-LLs and show that a *uniform* Semenoff mass cannot explain the observed spectrum. Starting from the linear dispersing bands in the Dirac cone without any magnetic fields, a mass term opens a gap at the Dirac point. The size of the gap is equal to *twice* the size of the mass term M. Experimentally, the existence of an inversion-breaking potential – responsible for such a mass term – has been proposed previously in the graphene on SiC sample system (*17*). It manifests in our ARPES cuts through the Dirac point by extending the linear dispersions of the lower and upper cones, for both sides with respect to the K point (fig. S3A), in that these extrapolations do not meet in a single point, but are offset from each other. To accurately determine the size of the gap, we fit two Lorentzians with a constant background to momentum distribution curves (MDCs) in the
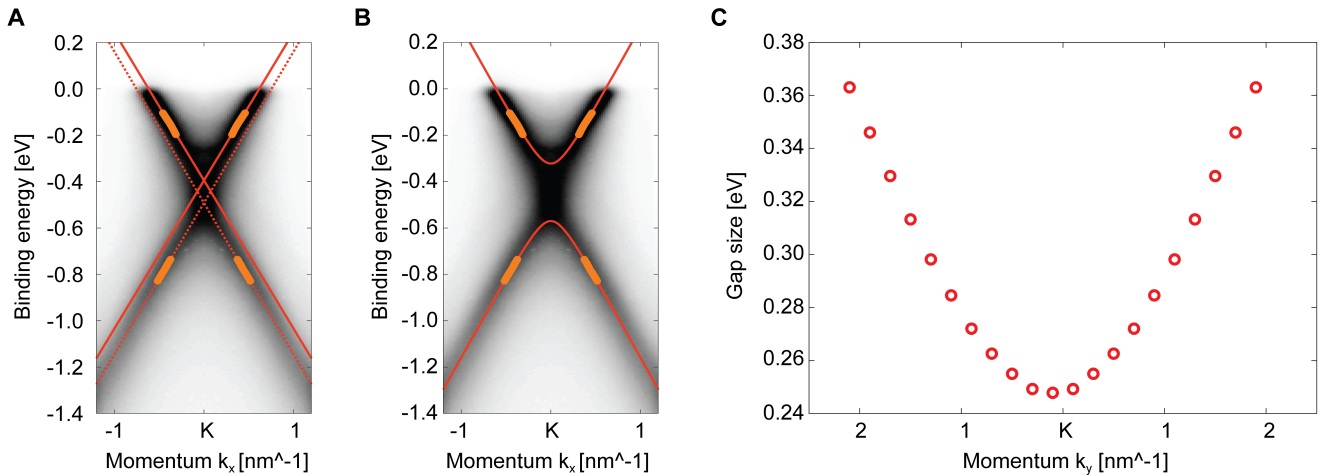

Fig. S3. Determination of the mass term. (**A**) ARPES cut through the Dirac cone. Orange circles indicate the positions of the fitted Lorentzians. The red line and the dashed red line indicate linear fits through the orange circles for the upper and lower cone respectively. The cut is symmetrized around the K point in the momentum direction to remove polarisation effects. (**B**) The same data as in (**A**), but fitted to a hyperbola instead. (**C**) Results for the gap size from the hyperbola fits for different ARPES slices along k_y. The curve shows the expected half-hyperbola and the gap size of $\sim$0.25 eV is given by the minimum.
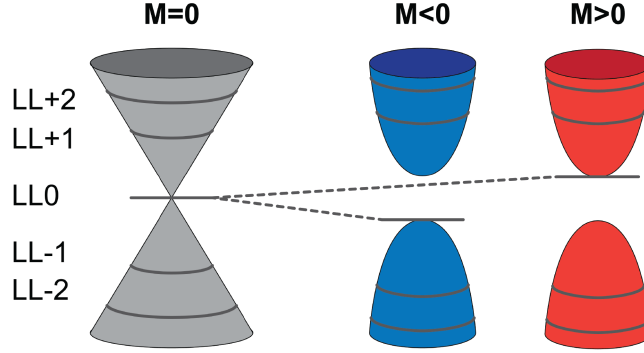
Fig. S4. Sketch of pseudo-LLs with Semenoff mass. Depending on the sign of the mass term M, the zeroth LL (LL0) gets shifted to the upper or lower part of the cone. The spectrum is identical for valleys K and K', because pseudomagnetic fields preserve time-reversal symmetry. Higher LLs only get pushed away slightly from the Dirac point.

upper and lower cones. The energy range of the fit is selected to avoid the prominent LLs. A hyperbola is then fitted to the bands (fig. S3B) to determine top and bottom of the two bands, and in turn the gap size. The procedure is repeated for several cuts through the Dirac cone along the k_y direction. The results are summarized in fig. S3c and the mass term is equal to half of the minimal gap size ($\sim$0.25 eV). This is comparable to the $\sim$0.26 eV gap observed in the same sample system by Zhou *et al.* (*17*).

Next, we describe the effects of a mass term on a Dirac dispersion including magnetic fields. In this case the zeroth LL (LL0), which normally resides at the Dirac point, is gapped out and shifts by an energy equal to the mass term. Note that Eqn. 2 is not properly defined for $n = 0$ To understand whether LL0 is shifted to $+M$ or $-M$ (in valleys K and K'), we have to distinguish between real magnetic fields, which break time-reversal symmetry, and pseudomagnetic fields, which preserve time-reversal symmetry. For real magnetic fields (*50*), LL0 has opposite energy $\pm M$ at K and K'. For pseudomagnetic fields, in order to preserve time-reversal symmetry, the spectrum must be identical in both valleys, and the energy of LL0 is determined by the sign of M, so for $n = 0$ we simply get $E_{LL0} = E_{DP} \pm M$. This is illustrated in fig. S4 for different
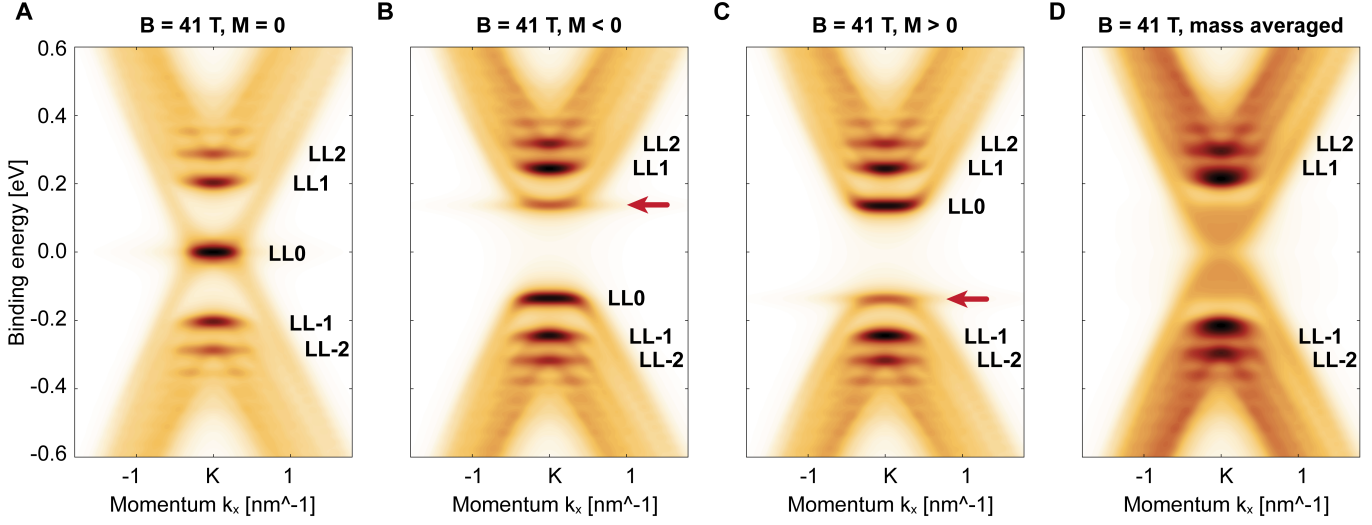
Fig. S5. Calculation of pseudo-LLs with Semenoff mass. Calculated spectral function in our triangular flake with a uniform pseudomagnetic field $B = 41\,\text{T}$ and Semenoff masses $M = 0$, $M = -135\,\text{meV}$, $M = +135\,\text{meV}$, and averaged in the interval $M \in [-135, 135]\,\text{meV}$ (from left to right). The position of the Landau levels (LL) for the different cases is indicated, as well as the much weaker LL0 from the area surrounding the strained flake (red arrows in (**B**) and (**C**)).

signs of the mass term, where LL0 either shifts to the top of the lower cone ($M < 0$) or the bottom of the upper cone ($M > 0$).

Our numerical simulations clearly show this behaviour (fig. S5), but there is one additional caveat. The total pseudomagnetic flux must be vanishing in our flake by construction, as we require the strain to relax at the edges of the flake. This requirement generates a region near the boundaries of the strained area with a pseudomagnetic field of the reversed sign. This region hosts a LL0 at an energy inverted with respect to the LL0 coming from inside the strained area. This is visible in our calculations as weaker and more broadened (in momentum) levels, indicated by red arrows in figs. S5B and S5C. Note that experimentally a similar scenario is natural on our graphene on SiC samples as well. The strain inside the nanoprisms needs to relax away from the feature, thus creating an area with an inversed pseudomagnetic field.
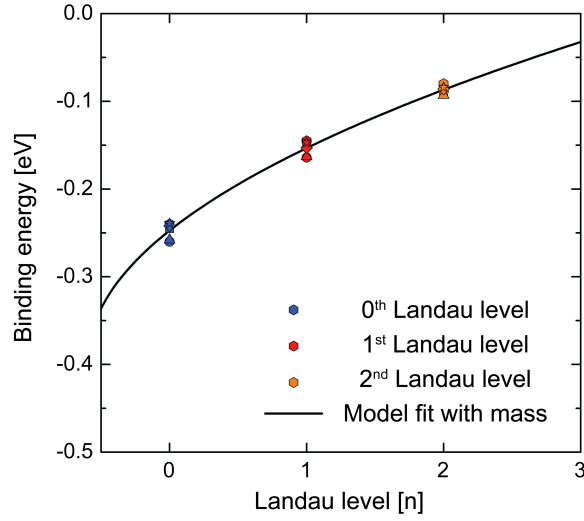
Fig. S6. Model fit with constant mass term. Fit of the observed LLs to Eqn. 2. Note the shifted indices for the LLs in this scenario. It places the Dirac point at a binding energy of 390 meV with $M = 150$ meV, compared to 450 meV obtained from the fit to Eqn. 1 without a mass term.

To check if a *uniform* mass term of about the determined size can explain our findings, we fit the observed LLs to Eqn. 2 (see fig. S6). While this model produces a qualitatively good fit with $M = 150$ meV, it places the Dirac point at a binding energy of 390 meV, which is inconsistent with the experimental observations (compared to 450 meV obtained from the fit to Eqn. 1 without a mass term). Hence, in order to explain the absence of a sharp LL0 in the ARPES data, we instead postulate that the mass term M varies slowly with respect to the magnetic length l_B, as discussed in the main text. This variation can take place either from nanoprism to nanoprism, or within a given nanoprism, if it is tied to the length scale of the uniform pseudomagnetic field λ. In this scenario, we can approximate the effect of the slowly-varying mass term M by averaging over the spectral function obtained with different fixed M (such as those shown in figs. S5B and S5C). This mechanism completely smears out LL0, while only slightly broadening the other levels (see fig. S5D).

4. Additional ARPES data

ARPES data for two additional samples complementary to the data in Fig. 2 is shown in fig. S7 with LLs indicated in the cuts along the energy axis. The data have not been symmetrized and the LLs are still clearly visible in the energy cuts. While the APRES data in the
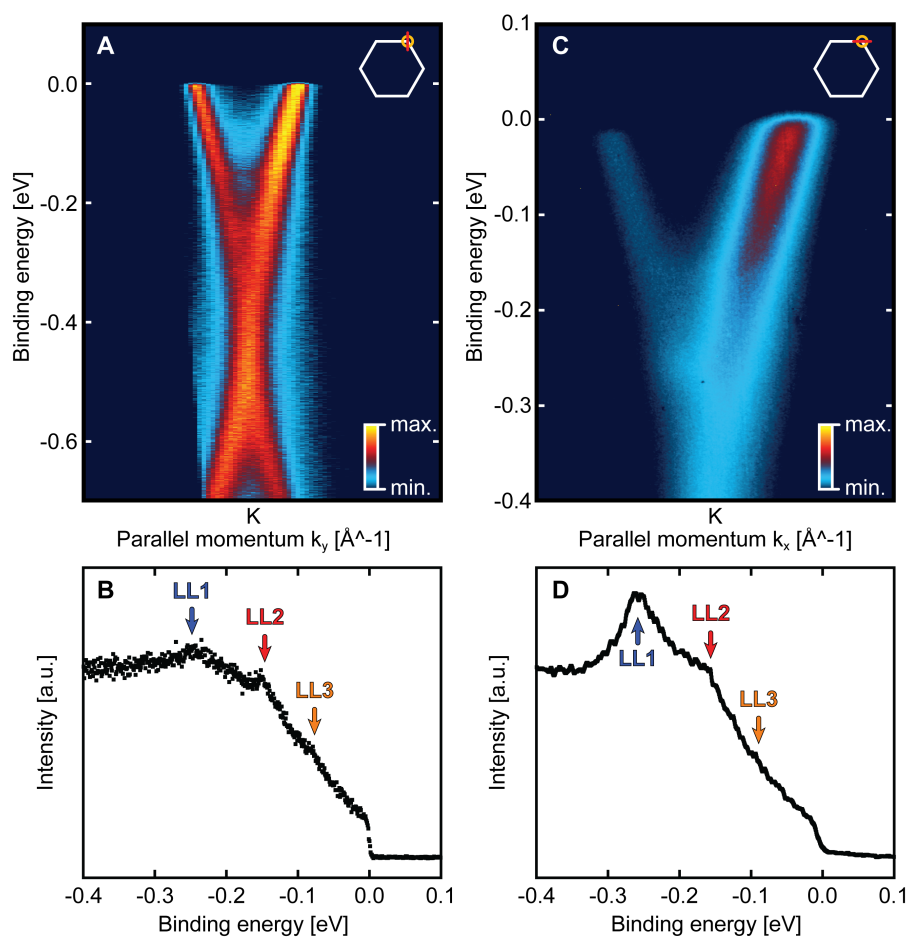

Fig. S7.   ARPES data on two additional samples. (**A**) ARPES cut along the direction indicated by the red line in the schematic BZ in the top right corner. Data were taken at 6 K with mostly unpolarized light. (**B**) Energy cut through the Dirac point of the data in (**A**) with LLs marked with arrows. (**C**) ARPES cut along the direction indicated by the red line in the schematic BZ in the top right corner. Data were taken at 6 K with p-polarized light. (**D**) Energy cut through the Dirac point of the data in (**C**) with LLs marked with arrows. Both data sets are unsymmetrized.

main text (Fig. 2A) were acquired with s-polarized light, the data in fig. S7A were taken with mostly unpolarized light, and the data in fig. S7C were taken with p-polarized light. The different light polarizations change the ARPES intensity distribution due to matrix element effects, but do not alter the position of the observed LLs in the energy cuts. For unpolarized light an almost symmetric intensity distribution for both branches of the Dirac cone can be observed, even without additional symmetrization (see fig. S7A).

5. Nanoprism distribution and step edge

Looking at the height distribution of the pixels in the AFM image in Fig. 1B (Top), we can determine the depths of the nanoprisms as well as estimate the coverage of the nanoprisms on the sample (fig. S8). The difference in the position of the two fitted Gaussians leads to a depth of the nanoprisms of (2.7 ± 0.7) Å. The integrated fraction curve indicates that about 5% to 10% of the total area is covered with nanoprisms.
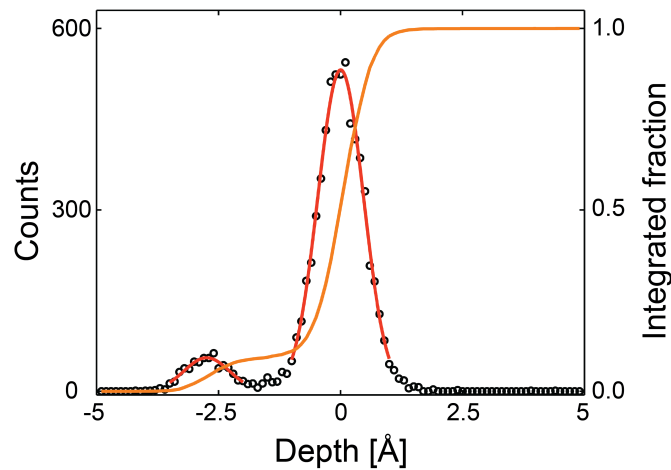

Fig. S8. AFM height distribution. Height distribution for the AFM image in Fig. 1B (Top). Two Gaussians (red) can be fitted to the data to extract the depths of the nanoprisms. The integrated fraction curve is shown in yellow.
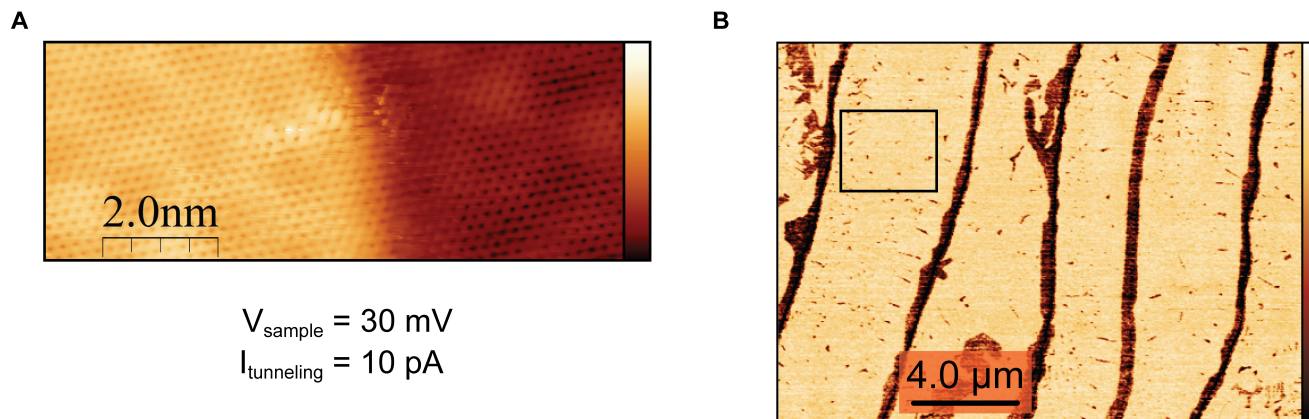
A

2.0nm

V_{sample} = 30 mV
$I_{tunneling}$ = 10 pA

B

4.0 µm

Fig. S9. Graphene layer coverage. (**A**) STM image taken across the edge of a nanoprism ($V_{sample} = 30\,\text{mV}$, $I_{tun.} = 10\,\text{pA}$). The graphene grows smoothly over the step without interruption. (**B**) AFM adhesion image taken in the same region as shown in Fig. 1A in the main text. The image shows no contrast between the nanoprisms and the surrounding terraces (black box), thus clearly indicating that the nanoprisms are covered by monolayer graphene.

The STM image taken across the edge of a nanoprism in fig. S9A shows how the graphene grows smoothly over the step without interruption. This assures that the strain inside the nanoprism can build up and is not relieved along grain boundaries. Adhesion measurements (see Methods section) unambiguously distinguish between coverages by zero-, mono-, and bilayer graphene (*51,52*). The AFM adhesion image in fig. S9B (taken in the same region as in Fig. 1A) shows no contrast between the nanoprisms and the surrounding terraces, thus clearly indicating that the nanoprisms are covered by monolayer graphene.